NANO · MICRO small
www.small-journal.com

Interplay Between Calcination Temperature and Alkaline Oxygen Evolution of Electrospun High-Entropy $(Cr_{1/5}Mn_{1/5}Fe_{1/5}Co_{1/5}Ni_{1/5})_3O_4$ Nanofibers

Keti Vezzù, Claudia Triolo, Kaveh Moulaee, Gioele Pagot, Alessandro Ponti, Nicola Pinna, Giovanni Neri, Saveria Santangelo,* and Vito Di Noto**

Spinel-structured transition metal (TM) oxides have shown great potential as a sustainable alternative to platinum group metal-based electrocatalysts. Among them, high-entropy oxides (HEOs) with multiple TM-cation sites are suitable for engineering octahedral redox-active centers to enhance the catalyst reactivity. This paper reports on the preparation of electrospun $(Cr_{1/5}Mn_{1/5}Fe_{1/5}Co_{1/5}Ni_{1/5})_3O_4$ nanofibers (NFs) and their evaluation as electrocatalysts. Its main aim is to unveil the nanostructural features that play a key role in the alkaline oxygen evolution reaction. Differing calcination temperature (300—800 °C) and duration (2 or 4 h) leads to different morphology of the NFs, crystallinity of the oxide, density of defects, and cation distribution in the lattice, which reflect in different electrocatalytic behaviors. The best performance (overpotential and Tafel slope at 10 mA cm^{-2}: 325 mV and 40 mV dec^{-1}, respectively) pertains to the NFs calcined at 400 °C for 2 h. To gain a deeper understanding of their electrocatalytic properties, the pristine NFs are investigated by a combination of analytical techniques. In particular, broadband electric spectroscopy reveals that the mobility of oxygen vacancies in the best electrocatalyst is associated to very fast local dielectric relaxations of metal coordination octahedral geometries and experimentally demonstrates the key role of O-deficient octahedra.

1. Introduction

In recent years, due to the high economic and social impact of climate changes, the attention of the scientific community has focused on achieving carbon neutrality. As a clean and efficient energy source, hydrogen could help bring the World to net zero emissions in the coming decades. Hence, it is one of the important vectors for building a sustainable energy system in the future. The generation of H_2 via the electrochemical splitting of water is a promising technology.[1–4] The efficiency of this process is a crucial factor for its practical application. In particular, the oxygen evolution reaction (OER) kinetically slower than the hydrogen evolution reaction (HER), represents the bottleneck of the water splitting (WS) process. Expensive platinum group metal (PGM)-based electrocatalysts are commonly utilized in both HER and OER.[5–9] Therefore, to favor the achievement of carbon neutrality

K. Vezzù, G. Pagot, V. Di Noto
Section of Chemistry for the Technology (ChemTech)
Department of Industrial Engineering
University of Padova
Via Marzolo 9, Padova 35131, Italy
E-mail: vito.dinoto@unipd.it

C. Triolo, S. Santangelo
Dipartimento di Ingegneria Civile
dell'Energia
dell'Ambiente e dei Materiali (DICEAM)
Università "Mediterranea"
Via Zehender, Loc. Feo di Vito, Reggio Calabria 89122, Italy
E-mail: saveria.santangelo@unirc.it

The ORCID identification number(s) for the author(s) of this article can be found under https://doi.org/10.1002/smll.202408319

DOI: 10.1002/smll.202408319

C. Triolo, S. Santangelo
National Reference Center for Electrochemical Energy Storage (GISEL)
Consorzio Interuniversitario Nazionale per la Scienza e Tecnologia dei Materiali (INSTM)
Firenze 50121, Italy

K. Moulaee, G. Neri
Dipartimento di Ingegneria
Università di Messina
Contrada di Dio, Vill. Sant'Agata, Messina 98166, Italy
E-mail: gneri@unime.it

A. Ponti
Laboratorio di Nanotecnologie
Istituto di Scienze e Tecnologie Chimiche "Giulio Natta" (SCITEC)
Consiglio Nazionale delle Ricerche
Via Fantoli 16/15, Milano 20138, Italy

N. Pinna
Department of Chemistry & The Center for the Science of Materials Berlin
Humboldt-Universität zu Berlin
Brook-Taylor-Str. 2, 12489 Berlin, Germany

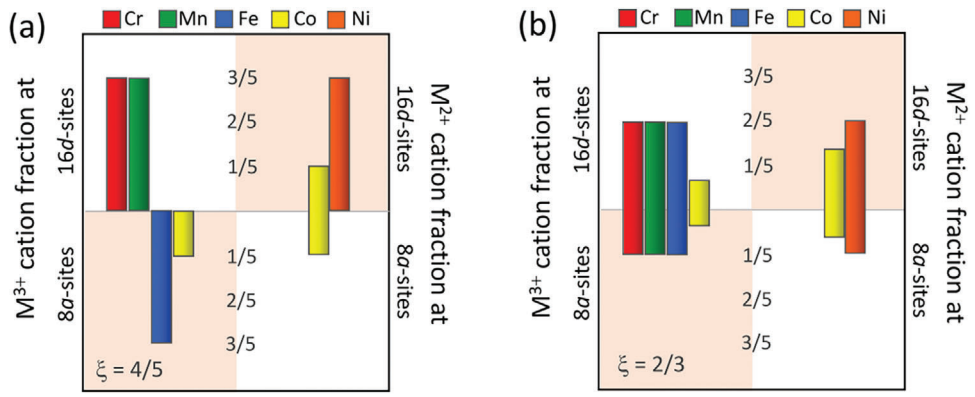

Figure 1. a) Equilibrium distribution of cations proposed for (Cr,Mn,Fe,Co,Ni) SHEO NFs obtained by calcination at high temperature (700 °C for 2 h, and then 900 °C for 2 h)[37] and b) completely random distribution of cations. ξ denotes the inversion degree of the spinel lattice.

in the short term, it is urgent to develop new catalytic materials, cheaper and/or more active toward HER and, in particular, OER. Spinel-structured oxides have shown great potential as a sustainable alternative to PGM-based electrocatalysts as they comprise Earth-abundant cations and are inexpensive, chemically reactive, thermodynamically stable and resistant to corrosion in alkaline environment.[10,11] Among them, those based on the high-entropy concept, benefiting from the synergy among their multiple metal components,[12,13] look like promising materials to replace expensive PGM-based electrocatalysts for OER in alkaline electrolyte. Several interesting results have been reported on spinel-structured high-entropy oxides (SHEOs)[12–20] Very recently, the evaluation of electrospun SHEOs as electrocatalysts in alkaline medium has evidenced that (Cr,Mn,Fe,Co,Ni) SHEO NFs outperform not only SHEOs based on different TM combinations, but also PGM-based oxides (such as IrO_2) commonly regarded as benchmark electrocatalysts.[21] Their good electrochemical performance has been attributed chiefly to oxygen vacancies (OVs) present on their surface and the occupation of octahedral sites by redox-active Co^{2+} and Ni^{2+} centers.[21] Therefore, by properly engineering the defects[12,13,22–28] and octahedral redox-active centers[29–31] further improvement can reasonably be achieved.

The presence of surface OVs, besides influencing the electronic structure and electronic conductivity of catalysts, is beneficial for OH^- adsorption and the charge transfer reaction during the OER process.[13,25,32–35] Dangling bonds or coordinately unsaturated atoms on the catalyst surface may provide increased amount of active sites to promote the electrocatalytic reaction.[36] cations occupying the octahedral and tetrahedral sites exhibit different electrocatalytic activity. The MO_6 octahedra possess higher degree of M—O covalence than the MO4 tetrahedra because of the higher electronic charge shared by O with.[30,31] The greater overlap between 3*d* and O 2*p* orbitals facilitates the electron transfer between the redox-active center of the oxide and oxygen, resulting in enhanced OER activity.[31] Moreover, the filling of the 3*d* orbitals split by the crystal field governs the binding strength of the OER intermediates.[25,29]

According to the cation distribution (CD) proposed by Ponti et al.[37] for (Cr,Mn,Fe,Co,Ni) SHEO NFs calcined at high temperature (700 °C for 2 h, and then 900 °C for 2 h), at thermal equilibrium (**Figure 1a**), Cr^{3+} and Mn^{3+} reside *only* on octahedral (16*d*) sites, as most frequently reported,[38,39] while all Fe^{3+} cations and 1/3 of Co^{3+} occupy tetrahedral (8*a*) sites; the remaining Co^{2+} and Ni^{2+} cations may accommodate both in 16*d* and 8*a* sites.[21,37] In the analogue CD proposed by Sarkar et al,[39] 1/3 of Ni^{3+} (in place of Co^{3+}) reside on tetrahedral sites. Calcination under milder conditions (at lower temperature and/or for shorter time) hinders the achievement of the equilibrium cation distribution (ECD). At low temperature or short duration of the heating treatment, the cations are close to being completely randomly distributed across the 8*a* and 16*d* sub-lattices, with 1/3 of each cation residing on the tetrahedral sites and 2/3 in the octahedral ones (Figure 1b). The variation in the distribution of cations in the 8*a* and 16*d* sub-lattices causes changes in the degree of inversion of the spinel oxide (ξ) and, more importantly, in the occupation of e_g orbitals at the octahedral sites and, hence, in the binding strength of OER intermediates.[29] Of course, these changes are accompanied by the variation of the crystallinity, morphology and surface properties of the fibers[40] that may also affect their electrochemical performance.

This work investigates the interplay between calcination conditions and electrocatalytic ability when (Cr,Mn,Fe,Co,Ni) SHEO NFs are used as anode for the alkaline OER, aiming at unveiling the nanostructural features that play a key role in the of the NFs anodic activity. Electrocatalysts are synthesized via the procedure described in a previous work.[21,37] Here, calcination is followed by rapid, uncontrolled cooling down to room temperature (RT) to generate abundant defects on the oxide surface.[41,42] Both temperature (300–800 °C) and duration (2 or 4 h) of the calcination process are varied and the interdependent changes produced by their variation in morphology of the NFs, crystallinity of the oxide, density of defects, and CD in the lattice are investigated to elucidate their influence on the electrocatalytic behavior of the fibers. For this purpose, the pristine NFs are thoroughly characterized by a combination of analytical techniques including broadband electric spectroscopy (BES). BES is a powerful technique used to study the electrical properties of materials over a wide range of frequencies, typically from millihertz to gigahertz. The principle behind BES involves applying an alternating electric field to the material and measuring its response in terms of complex permittivity and conductivity. This allows for the investigation of various polarization phenomena, including dipolar relaxations and charge transport mechanisms.[43–45] BES is particularly

effective for probing structural relaxations, interfacial polarization, and ion dynamics, providing valuable insights into the material's morphology, defects, and conductive pathways.[43–45]

In this paper, BES was applied for the first time to study SHEO NFs, revealing potential nanoscale heterogeneities such as nanodomains and their interfaces. The technique allowed for a detailed analysis of the relaxation modes within the structural network and an investigation of the interdomain conductivity pathways, thereby providing insight into the OER mechanism.

2. Results and Discussion

2.1. Physicochemical Properties of (Cr, Mn, Fe, Co, Ni) SHEO NFs

2.1.1. Morphology

Scanning electron microscopy (SEM), high-resolution transmission electron microscopy (HRTEM), high-angle annular dark-field scanning transmission electron microscopy (HAADF-STEM), energy-dispersive X-ray spectroscopy (EDX) x-ray diffraction (XRD), micro-Raman spectroscopy (MRS), and x-ray photoelectron spectroscopy (XPS) analyses were carried out to study the physicochemical properties of the calcined fibers. For an easy identification, in the following, the SHEO-electrocatalysts are labelled as ST_C/τ_C, with T_C and τ_C indicating temperature and duration of the calcination process (expressed in °C and in h, respectively).

Figure S1 (Supporting Information) summarizes the results of the SEM analysis. Regardless of the calcination conditions, micrometer-long NFs are formed upon heating treatment (Figure S1a–f, Supporting Information) from the as-spun polymer/TM-salts 1D templates, as in the case of (Cr,Mn,Fe,Co,Ni) SHEO NFs calcined at 700 °C for 2 h and then at 900 °C for 2 h.[21,37] However, their morphology changes markedly with T_C and τ_C. Fibers calcined at lower T_C are very long, thick and smooth (Figure S1a–c,g–i, Supporting Information). As T_C increases, the fibers become progressively shorter, thinner and rougher (Figure S1d,e,j–k, Supporting Information). Their diameter (d_{NF} in Table S2, Supporting Information) monotonically declines with T_C (Figure S1m, Supporting Information). At a given T_C, prolonging the duration of the heating treatment results in slightly thicker fibers (Figure S1f,l, Supporting Information).

TEM analysis (**Figure 2**a–o; Figure S2a–j, Supporting Information) reveals that all fibers have the granular structure typical of electrospun oxides.[21,37,40–42,46–51] This architecture facilitating electrolyte penetration and ion transport is beneficial for the OER activity.[52] As previously observed in other oxides,[49] the smoother fibers, formed upon calcination at lower T_C, consist of smaller-sized, densely-packed grains (Figure 2a–c,f–h; Figure S2f–h, Supporting Information) crystalline in nature (Figure S2k–o, Supporting Information), while the larger size of the grains in the fibers calcined at higher temperature/for longer time gives them a rougher appearance (Figure 2d,e,i,j; Figure S2i,j, Supporting Information). The expansion experienced by the polymer template and the contraction undergone by the TM-salts incorporated therein, occurring during calcination due to the degradation of the organic components, are responsible for the formation of spatially confined grains,[16,53] interconnected to build a porous architecture. Extensive overlap prevents reliable measurement of the size of the primary particles in the NFs calcined at T_C < 800 °C. In the case of S800/2 and S800/4 NFs, the particles are discernible due to much reduced overlap. In both S800/2 and S800/4 NFs, the particle size approximately is in the 60–100 nm range and the particles have shape ranging from polygonal shapes with straight edges and sharp vertices to smooth, round-shaped. The particles size is better determined by XRD techniques below.

Elemental mapping via STEM/EDX (Figure 2p–s; Figure S2p–s, Supporting Information) and projection analysis of the maps (Figure S3a–c, Supporting Information) evidence the spatially uniform distribution of the TM ions throughout all NFs at the nano-scale, confirming the formation of multicomponent solid solutions from the interconnected TM-network embedded in the polymer template when the organic components of the as-spun NFs are completely removed. In addition, by fitting the projected oxygen profiles (Figure S3d–f, Supporting Information) to models appropriate for solid or hollow NFs[37] information about the fiber cross section is inferred. Fibers calcined at lower T_C are mainly solid (Figure S3g,h, Supporting Information), while a channel along the fiber axis develops with increasing T_C and/or τ_C (Figure S3i, Supporting Information). Sintering effects occurring at higher temperatures are responsible for both the increase in oxide grain size and inner cavity formation. The above described changes are consistent with literature reports on the evolution of electrospun fiber microstructure promoted by the variation in T_C.[40]

2.1.2. Phase and Crystallinity of the Oxide

Figure 2k–o shows HRTEM images of the NFs. Analysis of the crystal fringes is only possible for non-overlapping particles at the edge of the NF tips. For all NFs, it is found that the analyzed particles are mostly single-crystals (polycrystalline particles are rare) with the spinel structure. The results of such analysis for the S400/2 and S800/2 NFs are shown in Figure S4 (Supporting Information).

Figure 3 displays the results of XRD and MRS analyses. Regardless of the calcination conditions, all reflections detected in the diffractograms of the NFs (Figure 3a) can be indexed to the spinel structure (JCPDS no. 22–1084).[21,37,54–59] The absence of secondary phase(s) and the formation of pure single-phase spinel are confirmed by Rietveld refinements from XRD data (Figure S5a–e, Supporting Information). This finding well agrees with the existence of a wide temperature-range for the formation of a single spinel-phase.[18] The evident narrowing of the XRD peaks accompanying the increase in T_C and/or τ_C (Figure 3a) proves that the variation of the calcination conditions affects not only the microstructure but also the crystallinity of the oxide nanograins. The average size of the SHEO crystallites (d_{SHEO} in **Table 1**) increases with increasing T_C (Figure S5a–e, Supporting Information) and/or τ_C, as expected.[38,60] The single-crystal nature of the particles detected by HRTEM (Figure S4, Supporting Information) and the qualitative agreement with the size of the SHEO grains (Figure 2k–o), allows to interpret d_{SHEO} as an average measure of the size of the SHEO particles. The crystallites forming the NFs are affected by microstrain at different level (Table 1),

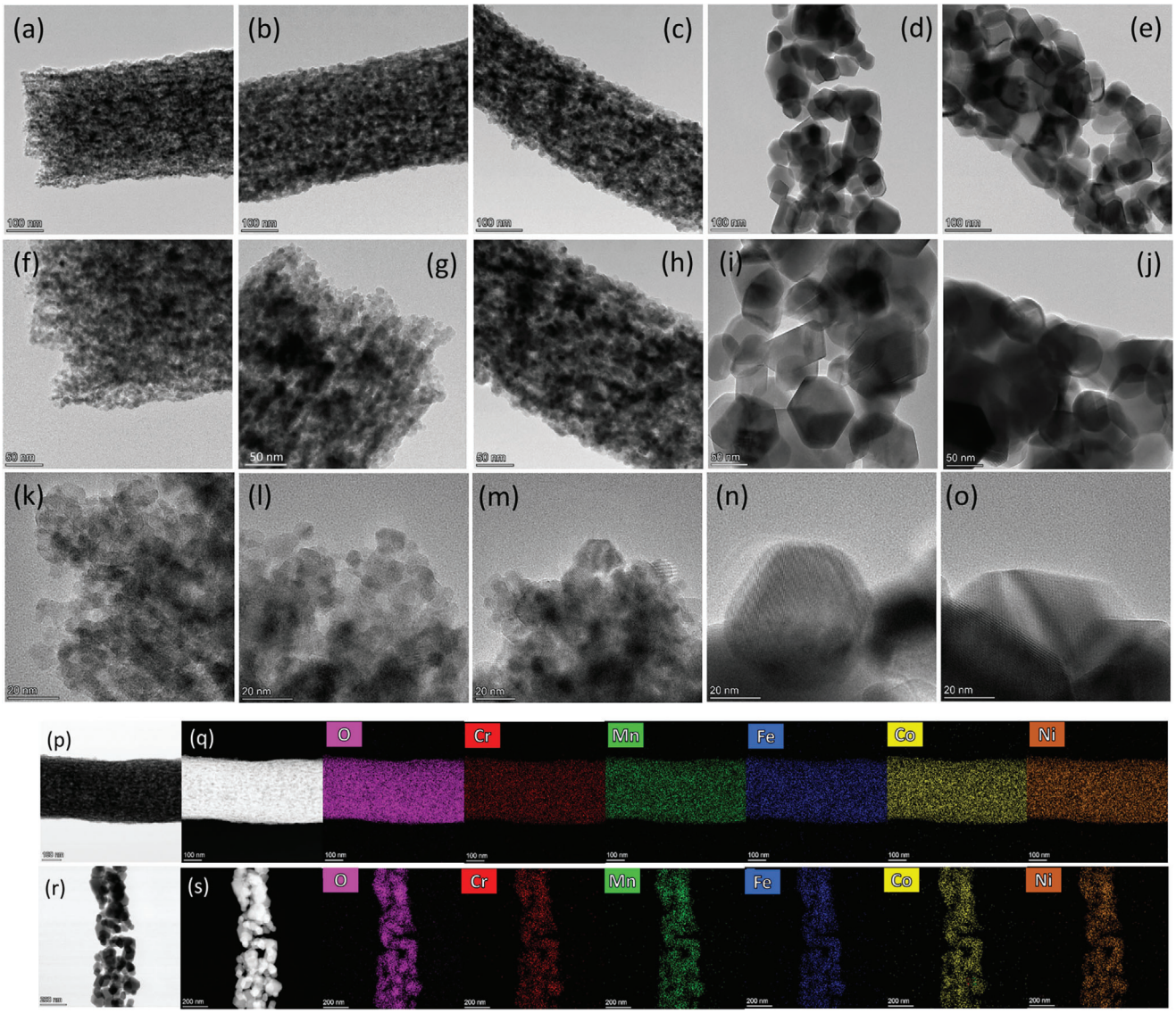

Figure 2. a–o) TEM images of electrospun NFs (a,f,k) S400/2, (b,g,l) S500/2, (c,h,m) S600/2, (d,i,n) S800/2, and (e,j,o) S800/4. (p,r) BF-STEM and (q,s) HAADF-STEM image of (p,q) S400/2 and (r,s) S800/2, followed by the correponding elemental maps.

but the latter seems not to be easily related to the calcination conditions

Electron diffraction (ED) patterns of all NFs are displayed in Figure S2k–o (Supporting Information). All diffraction rings can be indexed to the spinel structure and no other crystal phase is detected. The width and graininess of the diffraction rings clearly indicate the increase of the crystallite size when the NFs are calcined at higher temperature or for longer duration.

Figure 3b shows the micro-Raman spectra, as obtained by averaging those recorded at different random locations in each sample to evaluate the spatial homogeneity (Figure S6, Supporting Information). As discussed extensively in a previous paper,[37] five Raman-active normal vibration modes ($A_{1g} + E_g + 3F_{2g}$) are predicted for the spinel structure (*Fd-3 m* space group).[61–65] Their frequency positions and relative intensities strongly vary within the family of spinels.[66–69] The detection of broader and less resolved features in the spectra of fibers calcined at lower temperatures reflects the smaller coherence length (i.e., smaller *d*SHEO) in line with the literature.[38,60] In addition to the normal phonon modes, inversion-induced modes[14,63,70,71] also contribute to the Raman intensity in all samples (Figure S7, Supporting Information), in full agreement with both other reports on SHEOs[14] and previous studies.[21,37] Their relative intensity smoothly decreases with decreasing T_C (Figure S7, Supporting Information), indicating the occurrence of changes in the CD and the decrease of ξ, as expected (Figure 1). No significant shift of the peaks is observed.

2.1.3. Cation Distribution and Octahedral Occupation

The variation of the CD is accompanied by the change in octahedral occupation, which has a great influence on the

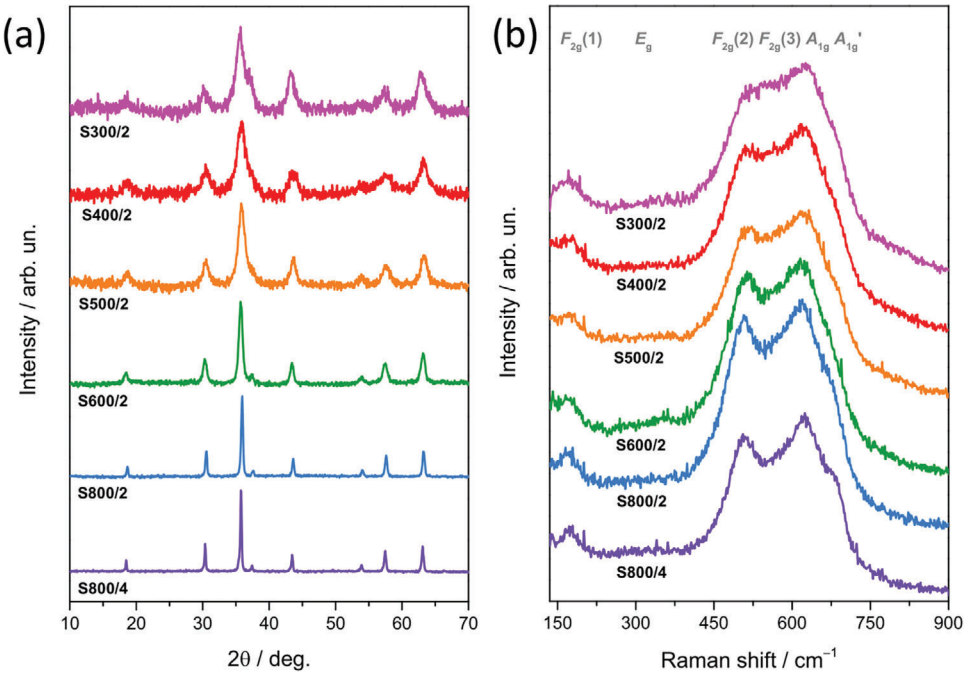

Figure 3. a) XRD patterns and b) averaged micro-Raman spectra of the samples.

electrocatalytic behavior of SHEO fibers.[21,51] Octahedral Co- and Ni-species exhibit higher reactivity towards OER than the remaining species.[72] Moving from the ECD (Figure 1a) to the completely random cation distribution (CRCD, Figure 1b), their total amount at 16*d* sites (4/5, referred to the M_3O_4 formula unit, FU) does not vary. Nonetheless, the octahedral occupation by cobalt species (Co^{2+} and Co^{3+}) increases from 1/5 to 2/5 and, correspondingly, the (Co^{3+}/Co^{2+}):Ni^{2+} ratio increases from 1:3 to 1:1. Assuming the distribution of cations proposed for (Cr,Mn,Fe,Co,Ni) SHEO by Sarkar et al.[39] as the ECD, similar considerations would apply to the Ni^{2+}, Ni^{3+}, and Co^{2+} cations. Einert et al.[20] have ascribed the electrocatalytic activity of mesoporous (Cr, Mn,Fe,Co,Ni) SHEO thin films to all cations residing on the 16*d* sites and specially to highly active Co^{3+} electrocatalytic centers. Conversely, He et al.[13] have proposed Ni^{2+} and Ni^{3+} as the most active centers in nano-porous $(Cr_{0.2}Mn_{0.2}Fe_{0.2}Co_{0.2}Ni_{0.2})_3O_4$. Hence, regardless of the CD assumed to be the ECD for (Cr, Mn,Fe,Co,Ni) SHEO (that proposed by Ponti et al.[37] or that proposed by Sarkar et al.),[39] the OER ativity is expected to benefit from the incomplete achievement of the ECD, as here demonstrated (see below) and as reported by He et al.[13] for $(Cr_{0.2}Mn_{0.2}Fe_{0.2}Co_{0.2}Ni_{0.2})_3O_4$ produced by low temperature solution combustion method.

Different occupation of 16*d* sites translates also in different occupation of e_g orbitals. The OER activity is strongly correlated with the occupation of e_g orbitals of surface TM cations in (pseudo)octahedral sites because the electrons in e_g orbitals can interact effectively with oxygen-containing adsorbates.[25] The e_g filling governs the binding strength of OER intermediates.[24,29] Lower (higher) filling results in stronger (weaker) adsorption of intermediates and more difficult (easier) desorption of O_2.[25] According to the widely accepted Sabatier principles of "optimum bond strength" for efficient catalytic reactions, the optimal OER activity is obtained at a moderate filling of the TM e_g orbitals ($e_g \approx 1$), which balances the competition between adsorption/desorption rate-limiting steps.[29] Thus, by properly modifying the occupation of e_g orbitals, the interaction between the adsorbate and active sites can be optimized. In the case of (Cr,Mn,Fe,Co,Ni) SHEO NFs, the optimal e_g filling, referred to the M_3O_4 FU, is 3. An e_g filling of 2.2 pertains to the ECD (Figure 1a), whereas for the CRCD (Figure 1b) the e_g filling increases to 2.8. Therefore, the more incomplete the achievement of the ECD is, the closer the filling of the e_g orbitals is to its optimal value.

Table 1. Results of Rietveld refinements: cell parameter (*a*), crystallite size (d_{SHEO}) and microstrain.

NF	*a* / nm	d_{SHEO}/ nm	Microstrain
S800/4	0.83437 ± 0.00006	82 ± 1	(3.7 ± 0.4) 10^{-4}
S800/2	0.83354 ± 0.00005	63 ± 1	(10.4 ± 0.5) 10^{-4}
S600/2	0.8321 ± 0.0002	20.9 ± 0.4	NS (2 ± 5) 10^{-4}
S500/2	0.8324 ± 0.0004	9.87 ± 0.05	(27 ± 4) 10^{-4}
S400/2	0.8342 ± 0.0008	6.5 ± 0.1	(7 ± 1) 10^{-4}
S300/2	0.837 ± 0.002	5 ± 3	NS (7 ± 9) 10^{-4}

NS: Not significant.

2.1.4. Surface Composition

The energetics for OER can be further optimized through the introduction of surface OVs.[12,13,21–28,51,73] Kim et al.[74] have shown that oxygen-deficient perovskite-type CaMnO2.5 produced by low-temperature synthesis outperforms stoichiometric CaMnO3

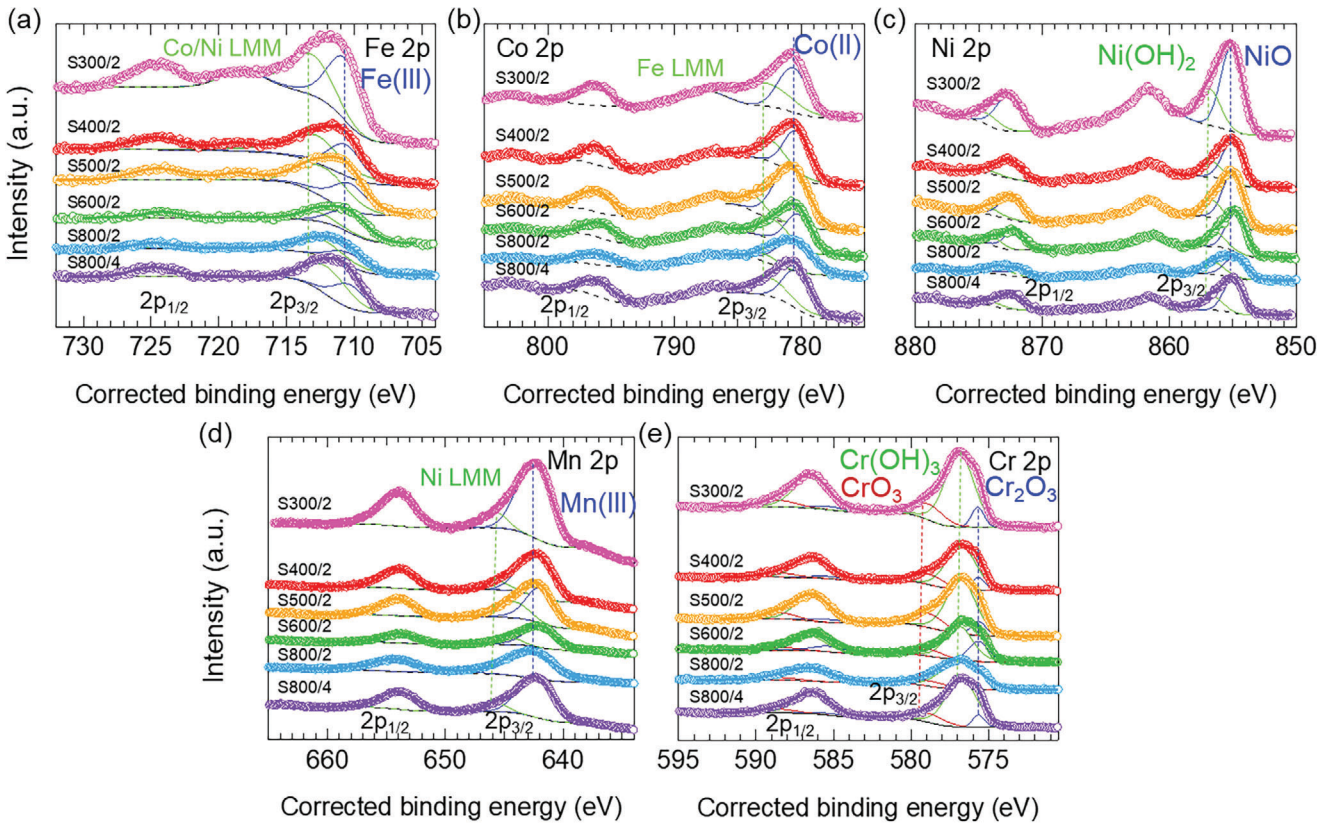

Figure 4. High-resolution XPS curves and fitting in the analyzed spectral regions: a) Fe 2p, b) Co 2p, c) Ni 2p, d) Mn 2p, and e) Cr 2p core levels.

as an electrocatalyst for alkaline OER. The presence of OVs on the catalyst surface results in larger exposure of the redox-active centers, changes in their electronic configuration from Mn4+($3d3$) to Mn^{3+}($3d^4$) with consequent increase of the e_g filling from 0 to 1.[74] Thus, the presence of surface OVs may further contribute to approach the optimal filling of the e_g orbitals. He et al.[13] have pointed out that in $(Fe_{0.2}Co_{0.2}Ni_{0.2}Cr_{0.2}Mn_{0.2})_3O_4$ with high grain boundary density the migration of OVs provides a convenient channel for electron transfer between different metal atoms.

According to Tao et al,[75] the surface reactivity of TM oxides increases with the density of coordinately unsaturated metal cations (M_{CUS}), i.e., with the density of OVs. Increasing M_{CUS} enhances/worsens the catalytic activity of TM oxides that weakly/strongly bind intermediates.[75] This is because the intermediates' bonding strength depends on the energy distance of the highest-occupied *d*-states from the Fermi level, which affects the filling of antibonding states.[25,75] As this distance reduces, antibonding states are pushed above the Fermi level and their filling diminishes leading to stronger adsorption. This change leads to an improvement (a worsening) in the case of adsorption-limited (desorption-limited) OER process.[25,75]

XPS survey spectra (Figure S7, Supporting Information) indicate the presence of cobalt, nickel, chromium, iron, manganese, oxygen and (adventitious) carbon on the surface of the SHEO-electrocatalysts. Elemental composition varies among different materials (Tables S3 and S4, Supporting Information), indicating that the temperature and duration of the calcination process has a fundamental role in inducing a selective migration of specific TMs towards the surface of proposed NFs. The Co surface concentration ranges between 18 and 33 relative at.%, with the maximum value achieved for samples calcinated at medium temperatures. On the contrary, the Ni surface concentration constantly decreases on T_C, in the range 16 to 25 relative at.%. The Cr surface concentration shows a specular trend with respect to Ni, with an exception for sample S800/2. The Fe surface content is the lowest among all the TMs and decreases from 12 to 8 at.% upon increasing T_C from 300 to 800 °C; it is 7 at.% for S800/4. Finally, Mn shows an opposite trend with respect to Co, with a minimum concentration for intermediate T_C. Indeed, a Mn surface concentration of 27, 18, and 33 at.% is determined for S300/2 and S400/2, S500/2 and S600/2, and S800/2 and S800/4 samples, respectively.

High-resolution XPS provides insights into the oxidation states of the surface elements in SHEO-electrocatalysts. It is important to note that the presence of Auger lines from different TMs may affect data accuracy in overlapping spectral regions. In the Fe $2p_{3/2}$ region (**Figure 4a**), a peak at ≈710.5 eV suggests that Fe species are present with a +3 oxidation state.[76,77] The second feature detected in this spectral region is assigned to the Co and/or Ni LMM Auger peak. Cobalt is present as Co(II), as highlighted by the appearance of a single peak centered at ca. 780.6 eV in the Co $2p_{3/2}$ spectral region (Figure 4b).[51,78] For S600/2 sample, this peak is shifted towards slightly lower binding energies (BEs, i.e., 780.2 eV), indicating a more reduced character of Co surface atoms for this material. An overlapping with the Fe LMM Auger peak is also observed. Differently from the previous

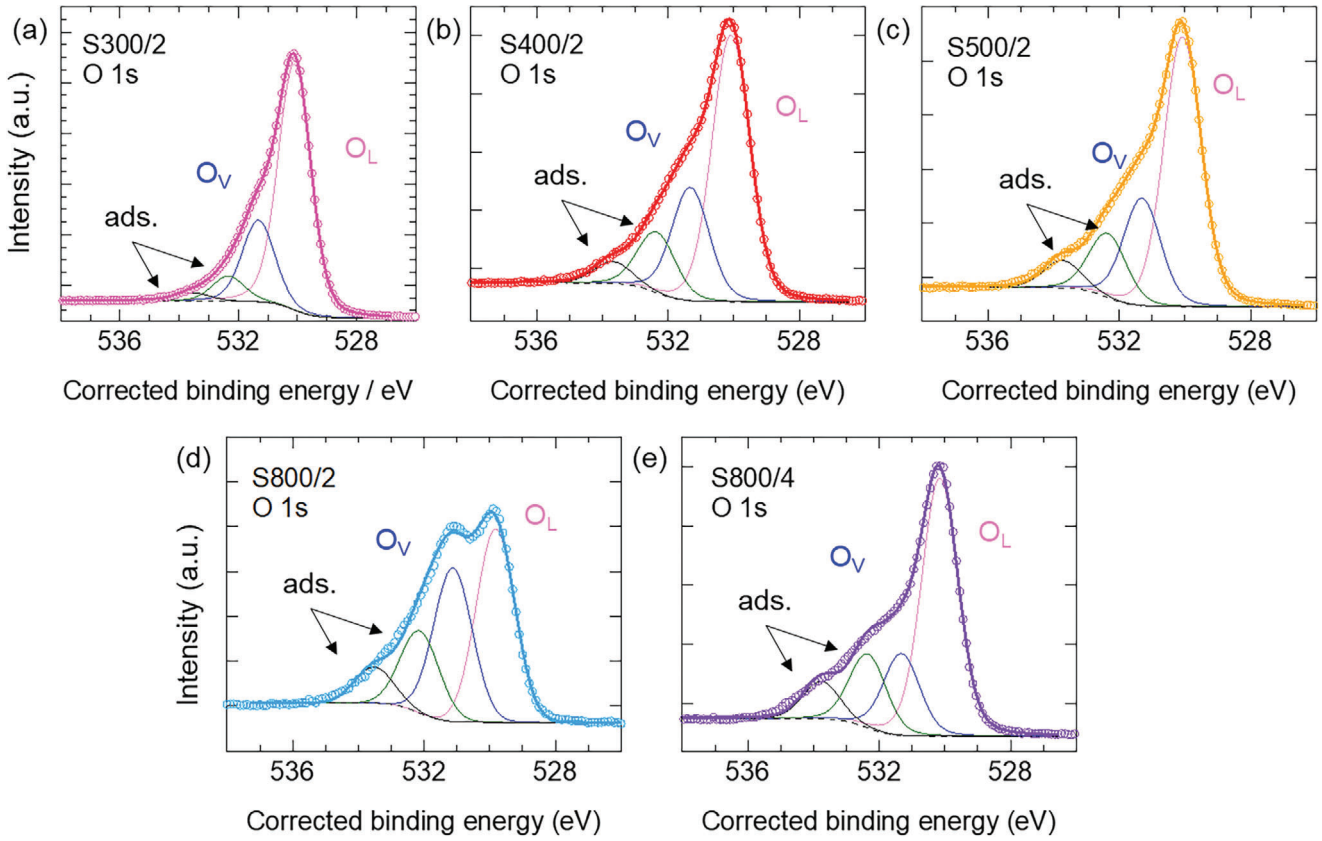

Figure 5. High resolution XPS curves and fitting in the O 1s spectral region for: a) S300/2, b) S400/2, c) S500/2, d) S800/2, and e) S800/4 samples.

metals, Ni $2p_{3/2}$ exhibits the presence of two different features centered at *ca.* 854.9 and 856.5 eV (Figure 4c), which can be assigned to NiO and $Ni(OH)_2$ species, respectively.[51,79,80] In the Mn $2p_{3/2}$ spectral region (Figure 4d), the two peaks at ≈642.1 and 645.7 eV are attributed to Mn(III) and Ni LMM, respectively.[12,51] The Mn $2p_{3/2}$ feature of S800/2 is shifted towards higher BEs (i.e., 642.8 eV), revealing that Mn surface atoms are likely in a +4 oxidation state.[81] Finally, the Cr $2p_{3/2}$ spectral region (Figure 4e) reveals that Cr surface atoms are present in three different chemical environments: i) Cr(III) oxide, with the peak centered at *ca.* 575.7 eV; ii) Cr(III) hydroxide, peaking at *ca.* 576.8 eV; and iii) Cr(VI) oxide, centered at *ca.* 578.9 eV.[51,82–84] In comparison with the bulk, Mn and Cr are more oxidized (beyond +III) and Co and Ni are more reduced (completely +II).

The O 1s spectral region of all samples exhibits four distinct features (**Figure 5**): i) at ≈530.0 eV, lattice oxygen atoms (O_L) are identified;[85–87] ii) at *ca.* 531.3 eV, a peak commonly associated with "*oxygen vacancies*" (O_V),[86,88] originates from surface O anions, proximate to lattice O_vs, passivated with hydrogen;[89] and iii) at higher BEs (i.e., 532.3 and 533.7 eV), features are ascribed to adsorbed or chemisorbed oxygen species like O_2 or H_2O.[21,37,90] The quantitative results detailing various oxygen species are summarized in Table S5 (Supporting Information). Overall, O_L is predominantly dominating all the samples. The O_V values asset at *ca.* 20 at.%. Interestingly, S800/2 sample lays outside the range, exhibiting an O_V value of 33 at.%. Analyzing the O_L/O_V ratio, extreme samples (i.e., S300/2 and S800/4) reveal a three-fold enrichment in O_L. Samples calcined at intermediate temperatures (i.e., S400/2, S500/2 and S600/2), exhibit an O_L/O_V value slightly higher than 2. In the case of S800/2, this value is 1.3. Except for S600/2 sample which reveals a different behavior, the amount of adsorbed oxygen-based species rises linearly with T_C (from 9 to 25 at.%), while the concentration of OVs exhibits a linear correlation with the $F_{2g}(2)/A_{1g}$ Raman intensity ratio (Figure S9, Supporting Information). Since the $F_{2g}(2)$ mode is ascribed to the asymmetric stretching mode of the TM−O bond in octahedron,[33,91] this finding (which is independent on the TM combination considered) might signal the increase of O-deficient octahedra.

2.2. Electrocatalytic Performance

The electrocatalytic performance of the (Cr,Mn,Fe,Co,Ni) SHEO NFs was investigated at RT in 1 M KOH electrolyte solution using a three-electrode setup. **Figure 6**a,b displays the polarization curves recorded in linear sweep voltammetry (LSV) and the Tafel plots (Figure 6b). The overpotential (η_{OER}) with respect to 1.23 V (equilibrium potential) needed to obtain a current density j = 10 mA cm^{-2} is adopted to depict the catalytic activity, whereas the kinetics of the reaction η_{OER}-driven is monitored by the slope (β_{OER}) of the Tafel curves (Table S6, Supporting Information).[15,21,92] β_{OER} does not significantly vary with the calcination conditions (inset of Figure 6b) and its value

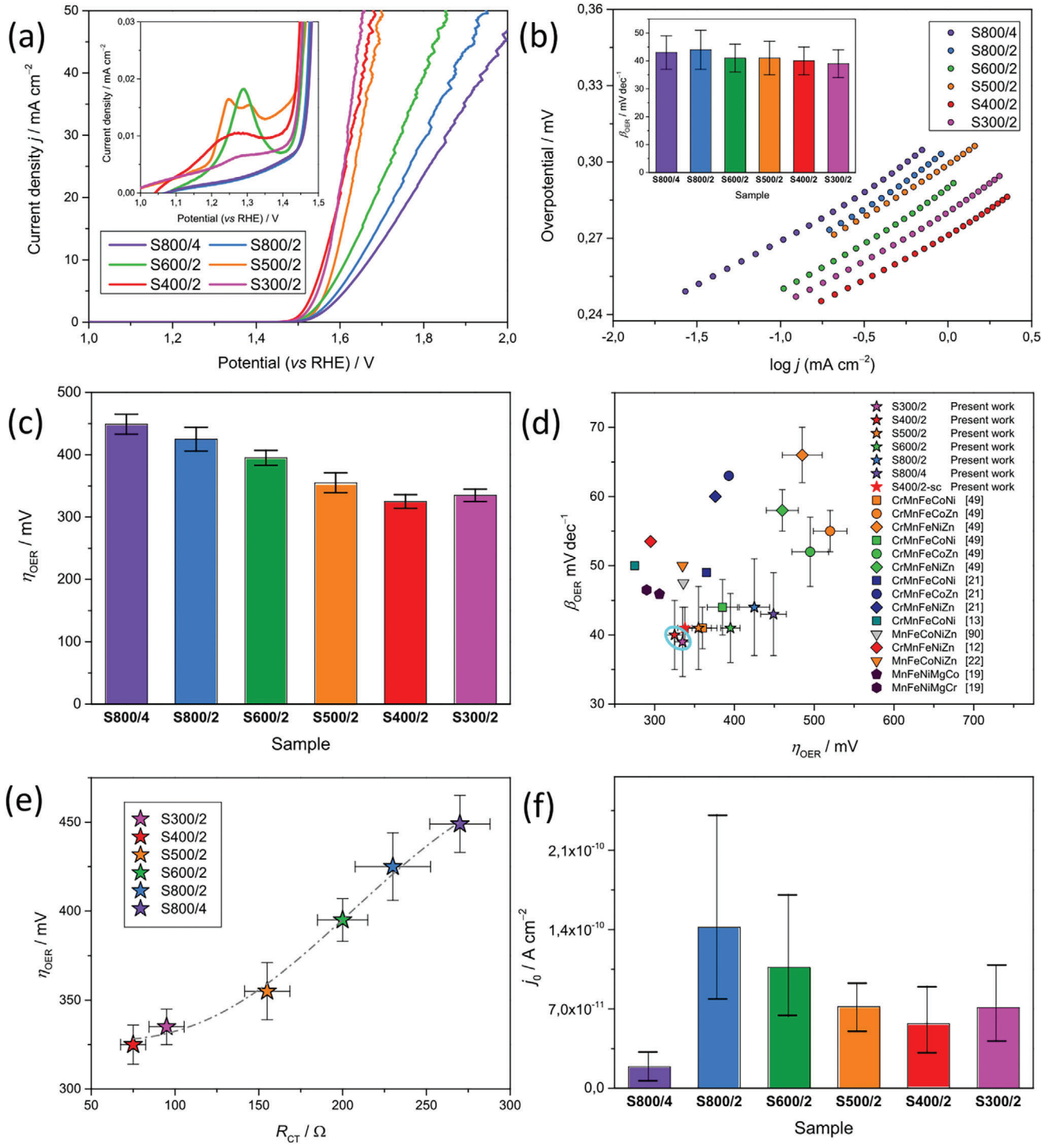

Figure 6. a–d) Results of the electrochemical measurements: a) LSV curves recorded at a scan rate of 5 mV s^{-1} in 1.0 M KOH (inset: pre-onset region) and b) corresponding Tafel curves (inset: Tafel slopes, β_{OER}). c) OER overpotentials (η_{OER}) measured at 10 mA cm^{-2}. d) Comparison with overpotentials and Tafel slopes reported in the literature[12,13,19,21,22,51,93] for high-entropy oxides based on various TM combinations (same color/shape indicates same synthesis temperature/TM combination; a cyan ellipse indicates the best performing SHEO NFs). e) Relationship between η_{OER} and charge transfer resistance (R_{CT}). f) Exchange current density (j_0).

(< 60 mV dec^{-1}) indicates that the OER is rate-limited by the production of O–O bonds on the catalyst surface.[12,49] On the contrary, the η_{OER} value needed to obtain 10 mA cm^{-2} lowers moving towards milder calcination conditions (Figure 6c). This finding, in line with the existence of an optimal catalyst calcination temperature,[94–96] proves the expected enhancement of the electrochemical performance and, hence, the successful catalyst designing. Remarkably, the best performing (S300/2 and S400/2) NFs outperform most of the high-entropy oxide-based electrocatalysts (Figure 6d) in terms of activity (lower η_{OER}) and/or kinetics (lower β_{OER}).

The charge transfer resistance (R_{CT}) at the electrolyte/electrode interface, as inferred from electrochemical impedance spectroscopy (EIS) measurements (Figure S11, Supporting Information), decreases in NFs calcined under milder conditions (inset of Figure S11, Supporting Information), most likely due to the shorter charge migration paths[97] provided by changes in NF architecture and properties. The increasing trend of η_{OER} versus R_{CT} (Figure 6e) suggests that the catalytic activity benefits from the decrease in polarization resistance. Besides, as shown in the case of S400/2, exhibiting the lowest η_{OER} and R_{CT} values, the catalysts are stable (Figure S12, Supporting Information).

In order to monitor the reaction kinetics at the equilibrium ($\eta_{OER} = 0$), the exchange current density (j_0) was determined by extrapolating the linear portions of the log(j) versus η_{OER} curves at $\eta_{OER} \to 0$ (Figure 6f).[98] Interestingly, the varying j_0 indicates that, different from the η_{OER}-driven kinetics, the equilibrium kinetics is strongly affected by the calcination conditions of the NFs.

2.3. Relationship Physicochemical Properties/Electrocatalytic Performance

In alkaline environment, OER is commonly assumed to proceed through a four-step proton-coupled electron transfer (PCET),[99] i.e., via the electrochemical adsorption of four hydroxide anions (OH^-) at the catalyst surface with release of four electrons (e^-), two water molecules and oxygen ($4\ OH^- \to 4\ e^- + 2\ H_2O + O_2$).[10,100] Different mechanisms have been proposed in the literature for the PCET, such as the adsorbate evolution mechanism[10,13,31,93,100–102] (AEM, Figure S13a, Supporting Information) and the lattice-oxygen mechanism[27,96] (LOM, Figure S13b, Supporting Information) or a combination of them.[24] AEM and LOM substantially differ in the nature of the active site (metal or lattice-oxygen, respectively). Here, oxygen-deficient octahedra MO_{6-x} on the SHEO surface are regarded as the active centers for the OER.[28,33,51,73] Accordingly, to evaluate the intrinsic activity of the catalysts, in the polarization curves (Figure 6a), the current density is normalized to the concentration of surface OVs (x_{OV}), which grows linearly with the amount of O-deficient octahedra (Figure S9, Supporting Information). The results, shown in Figure S14 (Supporting Information), reveal that higher intrinsic activity pertains to NFs (S300/2 and S400/2) calcined under milder conditions, while despite they possess the highest OV concentration, NFs S800/2exhibit the lowest intrinsic activity. The reason for this behavior will be clarified in Section 2.4.

Since OVs promote the adsorption for OH^-[13,28,51] and, thus, mediate the generation of bond between M_{CUS} and oxygen[28] (**Figure 7a**), an increase in x_{OV} is expected to produce an improvement in electrocatalytic performance, as already observed in previous studies on SHEOs[21,51] and reported for some (low-entropy) TM oxides.[25,28,35,75] Indeed, the increase of x_{OV} translates into a proportional increase in j_0 (Figure 7b): the higher x_{OV}, the faster is the equilibrum kinetics. Conversely, the plots of η_{OER}, β_{OER} and R_{CT} as a function of x_{OV} (Figure S15, Supporting Information), exhibit the typical shape of a volcano plot. This strongly suggests that x_{OV} is a valuable descriptor for the OER of the proposed spinels. It has been suggested that the migration of OVs provides a convenient channel for electron transfer between different metal atoms in the $(Fe_{0.2}Co_{0.2}Ni_{0.2}Cr_{0.2}Mn_{0.2})_3O_4$ electrocatalyst.[13] Thus, their surface density, rather than their total content, might control the η_{OER}-driven reaction. The surface density of OVs can be calculated as $\sigma_{OV} \cdot \approx x_{OV} \cdot {S_{SHEO}}^{-1}$, where $S_{SHEO} \propto {d_{SHEO}}^2$ is the surface area of a d_{SHEO}-sized grain. Actually, by plotting η_{OER} (Figure 7c), β_{OER} and R_{CT} (Figure S16, Supporting Information) as a function of the product of $x_{OV} \cdot {d_{SHEO}}^{-2}$, all data line up along common curves. Hence, the OV surface density *effectively* affects the electrochemical behavior of the SHEO NFs. The increase in σ_{OV} shortens charge migration paths, thus favoring charge transfer process. As a result, the polarization resistance lowers (Figure S12b, Supporting Information) and the overpotential needed to achieve 10 mA cm^{-2} decreases (Figure 7c), while reaction kinetics slightly fastens (Figure S16a, Supporting Information).

2.4. Broadband Electric Spectroscopy Analysis

The effects of OV charge transfer mechanisms and dielectric relaxation events within the host SHEO 3D inorganic structure on electrochemical performance are studied using BES. These studies focus on the S400/2 and S800/2 samples, which are selected for having significantly different electrochemical OER performance (Table S6, Supporting Information) and intrinsic activity (Figure S14, Supporting Information).

The electric response of S400/2 and S800/2 electrocatalysts was quantitatively analyzed as described in Section (Broadband dielectric spectroscopy). **Figure 8** shows the spectra of real component of complex permittivity ($\varepsilon'(\omega)$) and $tan\ \delta\ (\omega) = \varepsilon''(\omega)/\varepsilon'(\omega)$ of the two samples. The analysis revealed two polarization events (σ_{EP}, $\sigma_{IP,1}$) and four dielectric relaxation modes (f_1, f_2, $f_3$and f_4). σ_{EP} corresponds to the electrode polarization mode associated with the accumulation of charge at the interface between the sample and the electrode. $\sigma_{IP,1}$ is an interdomain polarization event attributed to the accumulation of charge at the interfaces between domains with different permittivity (or structural features) within the sample. This event reflects the potential structural heterogeneities at the mesoscale that characterize the samples.

The dependence of the two polarization events on the inverse of temperature, shown in **Figure 9**, reveals three temperature regions (I, II, III). In I, both σ_{EP} and $\sigma_{IP,1}$ profiles show Arrhenius-like behaviors, while in II and III a Vogel-Tamman-Fulcher (VTF) dependence is revealed. This demonstrates that, at the OER operating temperatures, long-range charge transfer mechanisms are modulated by diffusion of relaxation motions in the 3D network of the materials (i.e., by long-range coupling and migration

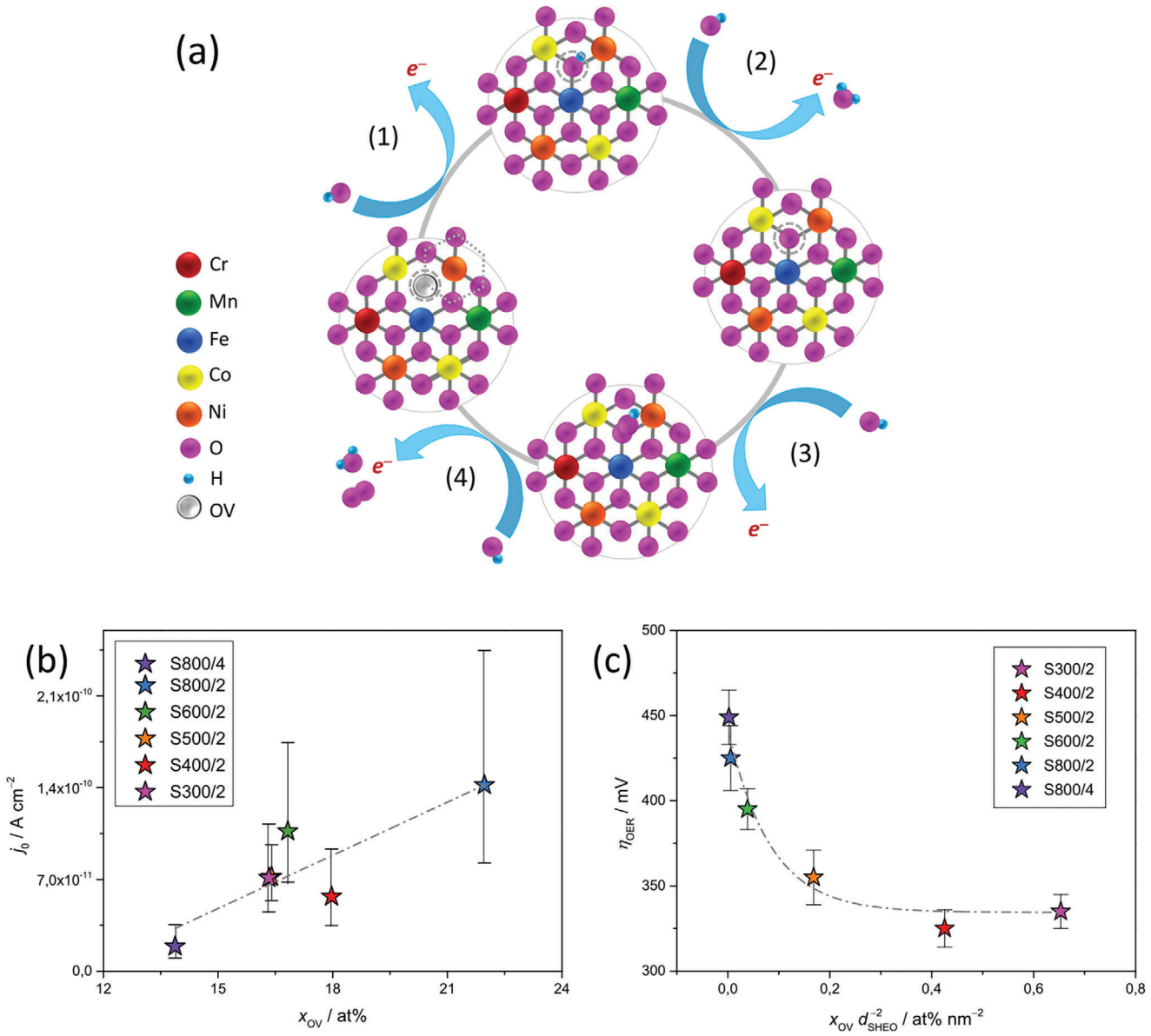

Figure 7. a) Sketch of the PCET for the OER in alkaline environment (inspired to ref. [13]): 1) * + OH^- → *OH + e^-; 2) *OH + OH^- → *O + H_2O + e^-; 3) *O + OH^- → *OOH + e^-; 4) *OOH + OH^- → * + H_2O + e^- + O_2, with * denoting the oxygen-deficient metal octahedra MO_{6-x} on the SHEO surface (dotted line) that act as the active centers for the OER; a dashed line marks an OV facilitating adsorption. b) Exchange current density (j_0) as a function of x_{OV} and c) OER overpotentials (η_{OER}) as a function of x_{OV} $d_{SHEO}{}^{-2}$, with x_{OV} and d_{SHEO} denoting atomic concentration of the surface OVs and average size of SHEO crystallites, respectively.

of dipole moment fluctuation events resulting from distortional states of MO_6 and MO_4 coordination units in the 3D spinel network of materials). As elsewhere described, the overall conductivity (σ_{tot}) of materials is the superposition of the two conductivity pathways ($\sigma_{tot} = \sigma_{EP} + \sigma_{IP,1}$). Figure 9 shows that: a) $\sigma_{EP} >> \sigma_{IP,1}$ and, thus, $\sigma_{tot} \sim \sigma_{EP}$; and b) in III and IV, $\sigma_{IP,1}$ of S400/2 is higher than that of S800/2 material. This indicates that OVs are highly mobile at the interface between domains with different permittivity.

In all regions, the overall conductivity of the materials is primarily modulated by the σ_{EP} contribution. This is due to long-range charge transfer processes that occur as a result of coupling with the long-range correlated diffusion of distortional states within the bulk medium of the host spinel 3D network. The S400/2 and S800/2 materials show no differences in terms of curve profiles and σ_{EP} values. This indicates that this charge migration event is not responsible for the significant difference in electrochemical performance exhibited by these two samples.

On the other hand, $\sigma_{IP,1}$, which is correlated to the mobility of OVs at the interface between domains with different permittivities, exhibits a significant difference in values between the S400/2 and S800/2 samples in regions III and IV. This result clearly demonstrates that the OER performance is directly

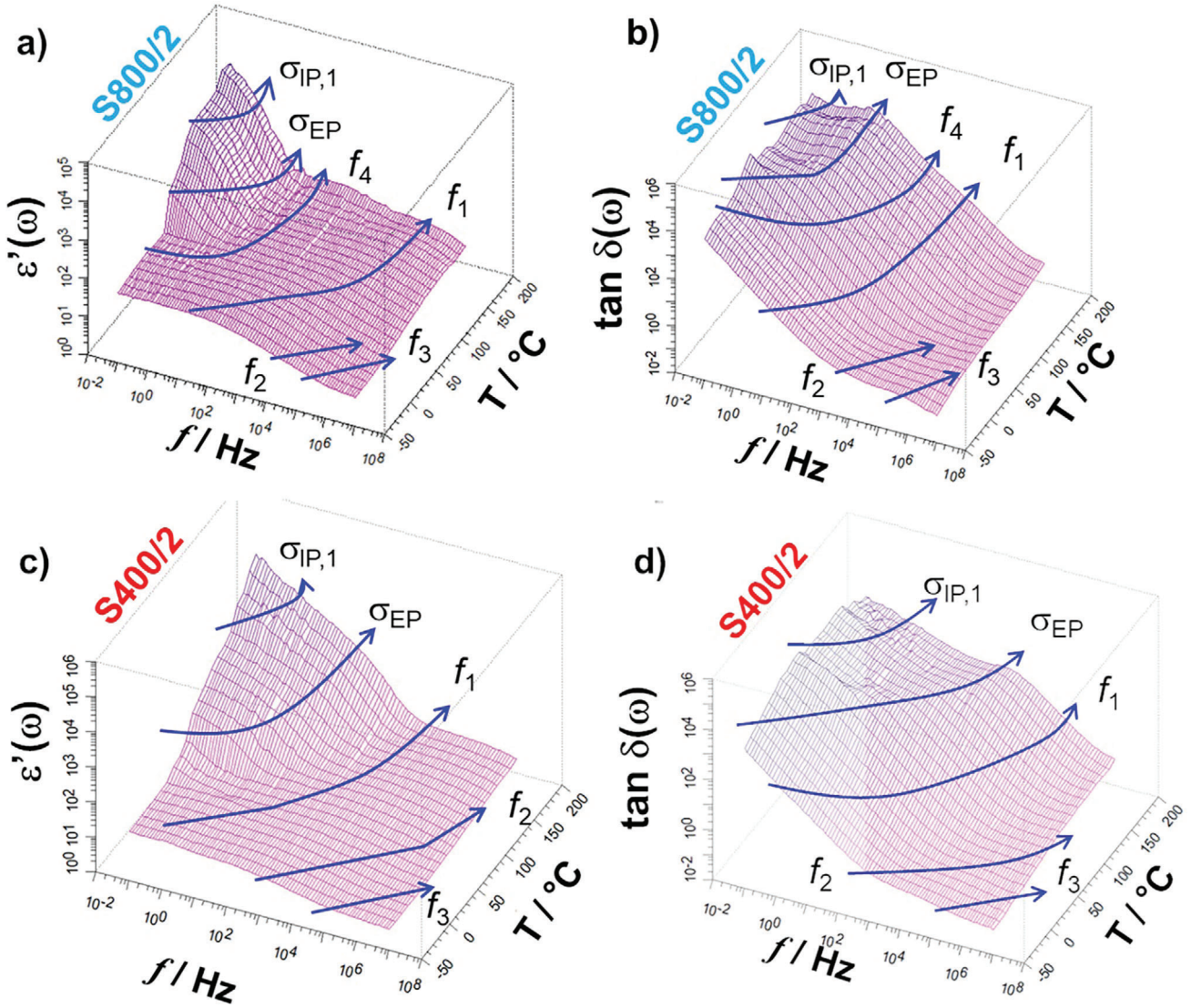

Figure 8. Spectra of real component of complex permittivity ($\varepsilon'(\omega)$) and *tan* $\delta(\omega)$ of S400/2 and S800/2 samples.

correlated to the surface mobility of the OVs present on the surface of the electrocatalysts.

The dynamics of the host spinel materials are investigated in depth by studying the dependence of the relaxation frequencies of the dielectric modes of the samples on temperature (**Figure 10**).

Four dielectric relaxations are detected, peaking at frequencies (f_1, f_2, f_3, and f_4). The frequencies f_1 and f_4 correspond to two long-range diffusion modes through the 3D spinel network, involving coupled distortional states of octahedral and tetrahedral metal oxide coordination units. The f_2 and f_3 modes are associated with local fluctuations of dipole moments in the distorted octahedral and tetrahedral units of the 3D network, respectively.

If one reasonably accepts that the electrocatalytic performance at room temperature of S800/2 and S400/2 is primarily associated with the fastest dielectric motions of the materials in regions II and III, the profile in Figure 10 clearly indicates that the dielectric modes correlated with this performance are f_1 and f_2 for the S800/2 and S400/2 samples, respectively. Notably, the values of f_1 (S800/2) are of the same order of magnitude as those of f_2 (S400/2), but it is important to note that:

(a) The long-range diffusion of coupled distortional motion in S800/2 (represented by f_1) actually *delocalizes* the distortional motion of the superficial complexes (Figure S17a and Video S1a, Supporting Information), thereby inhibiting their contribution to the electrocatalytic performance of this material. This accounts for the low intrinsic activity of NFs S800/2 despite them having the highest OV concentration (Figure S14, Supporting Information).

(b) In contrast, S400/2 exhibits a very fast *localized* distortional mode. This mode is attributed to the local fluctuations in the distortional motions of octahedral coordination TM geometries (Figure S17b; and Video S1b, Supporting Information),

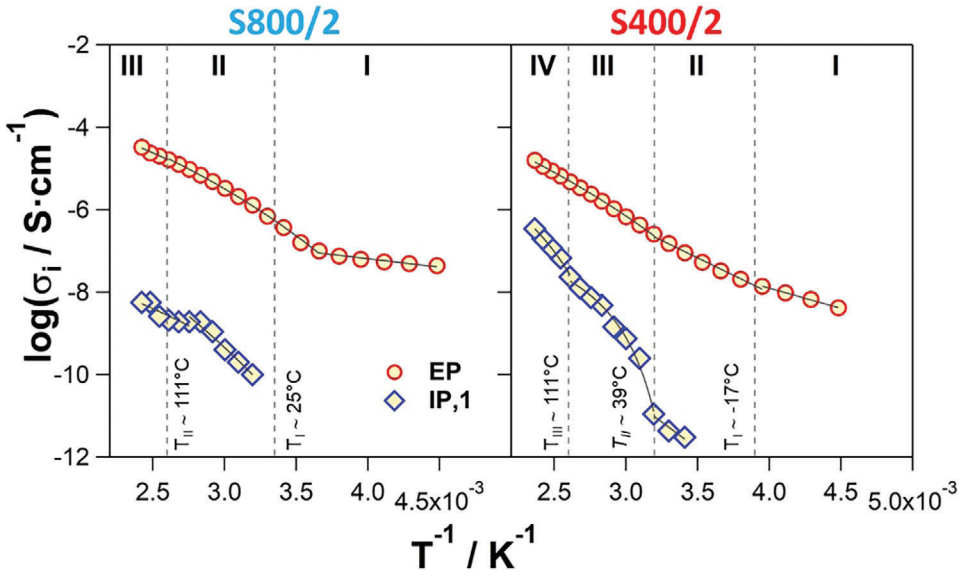

Figure 9. Dependence of σ_k for k = EP or IP,1 on temperature of S400/2 and S800/2 materials. Three temperature regions are revealed (I, II, and III).

which are highly effective for the OER process in this material, exhibiting very high intrinsic activity (Figure S14, Supporting Information).

Taking everything into account, the BES results shed light to the differences between the S800/2 and S400/2 samples. They suggest that, within this family of materials, a high OER rate is achievable when the electrocatalyst surface exhibits a high concentration of localized OVs, which correspond to very fast local dielectric relaxations of metal coordination octahedral geometries. Further confirmation of this evidence is obtained by analyzing the activation energy correlation map of polarization events σ_{EP} and $\sigma_{IP,1}$ and the dielectric relaxation modes (f_i), as depicted in **Figure 11**.

In S800/2, the activation energy of the overall charge transfer mechanisms is predominantly consistent with that of f_1. Therefore, in this case, the cooperative diffusion of distortional states of octahedral and tetrahedral coordination geometries within the 3D network of SHEO plays a crucial role in modulating the overall electric response of S800/2. On the other hand, in S400/2, the activation energy of the overall charge transfer mechanisms is preferentially correlated with f_2. This confirms that the electric response of this material is primarily associated with the *local* fluctuations of the dipole moments linked to the

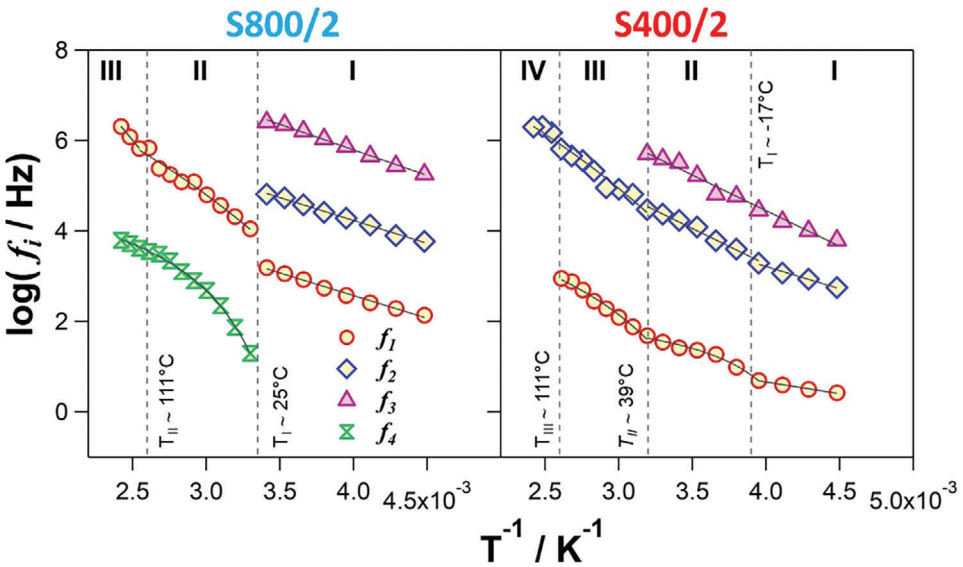

Figure 10. Temperature-dependence of dielectric relaxation frequencies (f_i, where i = 1, 2, 3, 4) of the S400/2 and S800/2 materials. The temperature regions I, II, III, and IV, as well as the delimiting temperatures (T_I, T_{II}, and T_{III}) are shown.

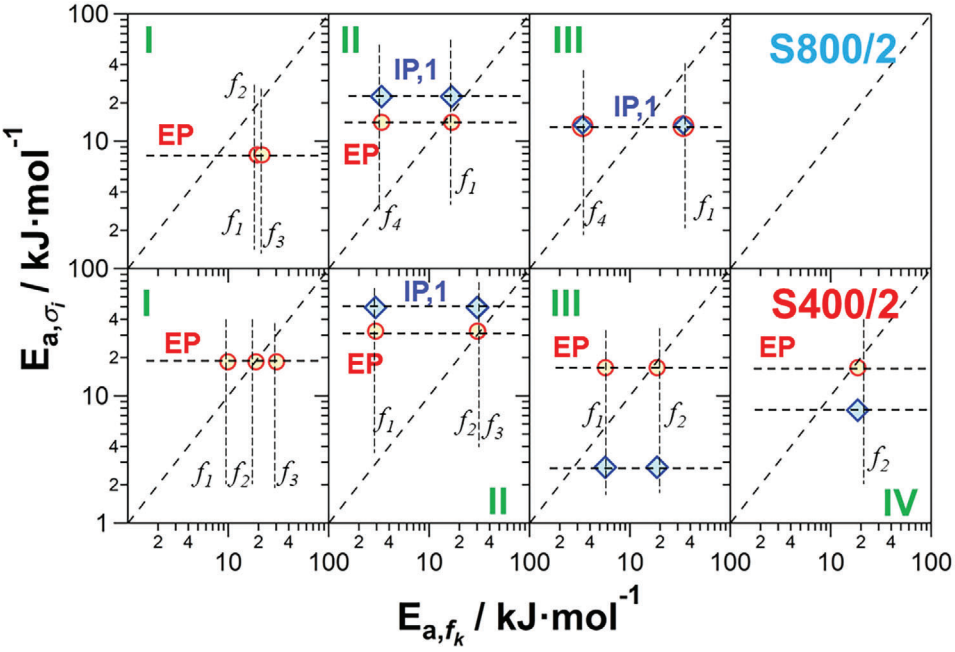

Figure 11. Relationship between activation energy of polarization events σ_{EP} and $\sigma_{IP,1}$ and the four dielectric relaxation modes (f_1, f_2, f_3, and f_4). The temperature regions I, II, III, and IV, along with the types of samples, are clearly indicated.

distorted octahedral units present on the surface of the spinel nanoparticles.

Thus, BES analysis allows accounting for the different electrocatalytic behavior of two OV-rich materials and, more importantly, evidences the key role of distorted octahedral units with localized OVs. The latter is a very general result, as defective (strained/distorted/O-deficient) octahedral units have been indicated as the active sites for OER in a wide variety electrocatlysts, regardless of their entropy (low or high), composition and lattice structure (spinel, perovskite, layered double hydroxides, etc.).[21,28,31–33,51,73,74,96,103]

3. Conclusion

Spinel-structure high-entropy (Cr,Mn,Fe,Co,Ni) oxide nanofibers are produced by electrospinning and calcination under different calcination conditions (temperature: 300–800 °C; duration: 2 or 4 h) and are evaluated as electrocatalysts for OER in alkaline environment. From the study of their physicochemical properties by means of SEM, TEM, XRD, XPS, and micro-Raman spectroscopy it emerges that the variation of the calcination conditions leads to different morphology of the fibers, crystallinity of the oxide, density of defects and cation distribution in the lattice. These changes reflect in different electrocatalytic behaviors.

At 10 mA cm^{-2}, $(Cr_{1/5}Mn_{1/5}Fe_{1/5}Co_{1/5}Ni_{1/5})_3O_4$ nanofibers calcined at 400 °C for 2 h exhibit the best electrocatalytic performance (overpotential and Tafel slope: 325 mV and 40 mV dec^{-1}, respectively). This behavior is understood in terms of beneficial changes in the charge migration paths, amount of oxygen-deficient octahedra MO_{6-x} active centers and e_g filling at the octahedral sites.

BES reveals that the structure and dielectric relaxations of the spinel 3D network play a crucial role in modulating its electrochemical performance. It demonstrates that this performance is correlated with the surface density and mobility of the distorted octahedral oxygen vacancies, which serve as a significant electrocatalytic descriptor for the OER process in the spinel materials.

Indeed, the results demonstrate that the 3D mobility of OVs is coupled with the structural relaxation of spinels. In particular,

(a) In the best performing S400/2, it is associated with the local dipole moments of the distorted octahedral coordination units present on the surface of the spinel nanoparticles.

(b) In S800/2, it corresponds to the long-range 3D diffusion of distortional states of both octahedral and tetrahedral coordination geometries in the materials.

4. Experimental Section

Synthesis of the Electrospun SHEO-Electrocatalysts: The SHEO-electrocatalysts were prepared by following the procedures illustrated in detail in a previous paper.[37] The precursor solution, based on an equimolar (Cr,Mn,Fe,Co,Ni) combination was prepared via sol-chemistry. Electrospinning was operated via a CH-01 Electro-spinner 2.0 (Linari Engineering s.r.l.). Calcination was carried out in a muffle furnace under conditions reported in Table S2 (Supporting Information); temperature was increased at a rate of 10 °C min^{-1}. Further details are given in the Supporting Information (SI).

Physicochemical Characterization: SEM, TEM, XRD, MRS, and XPS analyses were carried out to investigate the morphology, texture, microstructure, crystalline phase, and surface composition of the SHEO-electrocatalysts. A Phenom Pro-X scanning electron microscope and a FEI Talos F200S scanning/transmission electron microscope (operated at 200 kV and equipped with an EDX spectrometer for elemental mapping) were utilized to acquire the SEM images and carry out HRTEM, HAADF-STEM, and SAED analyses, respectively.

Detailed information on the NF morphology was inferred by projection analysis of STEM-EDX maps. Projection analysis consists in selecting a straight, constant-diameter NF (or region of a NF) and integrate (project) the map intensity along the NF axis. The so-obtained transverse projection was fitted to appropriate models:

$$I_{solid}\ (x) = I_b + I_0\sqrt{1-(x/R)^2}\ \ \text{(for solid NFs)} \tag{1}$$

$$I_{hollow}\ (x) = I_b + I_0\left(\sqrt{1-(x/R_{out})^2} - \sqrt{1-(x/R_{in})^2}\right),\ \text{(for hollow NFs)} \tag{2}$$

where I_b denotes the projected background intensity, I_0 is a constant depending on the NF size and composition, x indicates the distance from the profile center ($-R \le x \le R$), R stands for the radius of a solid NF, and R_{out} and R_{in} are the outer and inner diameter of a hollow NF, respectively.[37] In some cases, the solid and hollow model were not able to reproduce even approximately the projection profile. This occurs, for example, when the transformation from pristine NFs to hollow NFs was not complete due to brief, low-temperature calcination. An example of this can be seen in Figure S3a–f (Supporting Information), where the profile of S500/2, S600/2, S800/4 display solid, boxcar and hollow profiles. To model this intermediate situation, it was assumed that the NF density ρ depends on the distance r from the NF axis following a power law

$$\rho\ (r) = \rho_0 + (\rho_{out} - \rho_0)\ (r/R)^n,\ n \ge 0 \tag{3}$$

where r is the radial distance from the NF axis, ρ_0 and ρ_{out} are the density at the NF axis and surface, repectively, and n is a positive real number. Note that $n = 0$ corresponds to a solid NF. A power-law model was chose as it flexible yet simple enough to be analytically integrated as

$$I_{power-law}\ (x;n) = \begin{cases} I_b + I_0\sqrt{R^2-x^2}\,[\rho_0 + (\rho_{out}-\rho_0) \\ \times (x/R)^n\,{}_2F_1\left(\frac{1}{2}, \frac{-n}{2}; \frac{3}{2}; 1-(x/R)^2\right)\Big],\ x \ne 0 \\ I_b + I_0\left(\frac{\rho_{out} + n\rho_0}{n+1}\right),\ x = 0 \end{cases} \tag{4}$$

where ${}_2F_1$ is the Gaussian hypergeometric function and $-R \le x \le R$. Comparing how well the NF projections fit to the above models, one can get some insight into the NF internal structure and, in the power-law case, a quantitative estimate of the radial density profile.

XRD patterns were recorded with a Bruker D2 diffractometer using Ni β-filtered Cu-K_α radiation source ($\lambda = 0.1541$ nm). Raman scattering was measured by a NTEGRA—Spectra SPM NT-MDT confocal microscope coupled to a solid-state laser operating at 2.33 eV (532 nm) and delivering a power of 250 µW at the sample surface. The scattered light from the sample, collected by a 100X Mitutoyo objective (NA = 0.75), was dispersed by an 1800 lines mm^{-1} grating and detected by a cooled ANDOR iDus CCD Camera.

XPS analyses were conducted employing an EnviroESCA spectrometer (Specs) featuring an AlKα X-ray source ($h\upsilon$ = 1486.6 eV). The measurements were carried out under vacuum conditions at $\approx 10^{-6}$ mbar. High-resolution spectra were obtained with a pass energy of 50 eV, integrating for 0.1 sec $step^{-1}$, and recording data points at intervals of 0.1 eV $step^{-1}$. To address experimental errors stemming from charge accumulation, spectra were shifted in BE. A BE value of 284.8 eV was specifically applied to correct for the adventitious carbon.[104] Subsequent analysis involved decomposition of XPS curves utilizing the Keystone software (Specs) and adopting a Shirley-type background.[105] Quantification parameters were supplied by Specs.

Further details on the instrumentation can be found elsewhere.[37]

Electrochemical Characterization: Electrochemical measurements were performed at RT using a potentiostat/galvanostat workstation (AUTOLAB PGSTAT 204 instruments) and NOVA 2.1.5 software. A three-electrode set-up was used for this purpose with a platinum auxiliary (www.metrohm.com) counter electrode, an Ag/AgCl (www.metrohm.com) reference electrode and a catalyst-loaded screen-printed carbon electrode (SPCE, www.dropsens.com) acting as the working electrode. The OER catalyst solutions were prepared by mixing the catalysts (5 mg) with 5 wt.% Nafion solution (50 µL) and isopropanol (950 µL). KOH (1 M) in demineralized water was used as the electrolyte. Its pH (≈13.77) was measured by a pH meter. The catalysts were loaded onto the working area (4 mm in diameter) of SPCE; external reference- and counter-electrodes completed the circuit.

As usual,[13,106,107] Nernst equation, $E_{RHE} = E_{Ag/AgCl} + 0.0592\ pH + E^0{}_{Ag/AgCl}$ (with $E^0{}_{Ag/AgCl} = 0.198$ V), was used to convert the measured potentials, $E_{Ag/AgCl}$, into those referred to the reversible hydrogen electrode (RHE), E_{RHE}. Then, the overpotentials for the OER were calculated as $\eta_{OER} = E_{RHE} - 1.23$ V.

The polarization curves for OER were recorded in LSV mode and at a scan rate of 5 mV s^{-1}. The charge transfer resistance (R_{CT}) at the electrolyte/electrode interface was determined from the Nyquist plot recorded by conducting electrochemical impedance spectroscopy (EIS) in the frequency range from 1 Hz to 100 kHz at an applied potential of 1.7 V (vs RHE). Sinusoidal alternating voltages with an amplitude of 0.01 V (V_{rms}) were used. Experimentally measured potentials (vs Ag/AgCl) were corrected for the ohmic drop corresponding to the uncompensated solution resistance (R_u). The R_u value was extracted from Nyquist plots of EIS experiments.

Broadband Electric Spectroscopy: BES studies were carried out in the frequency range from 0.03 to 10^7 Hz using a Novocontrol Alpha-A analyzer over the temperature range from −100 to 150 °C. The temperature was controlled using a cryostat operating with a N_2 gas jet heating and cooling system and the temperature was measured with an accuracy greater than ±0.02 °C. The measurements were performed placing the sample between two Pt disk electrodes with a diameter of 13 mm. Samples were in the form of a pellet with thickness of ca. 1 mm. The cell was closed in a glovebox filled with argon and maintained under nitrogen during the measurements. The distance between electrodes was determined by using a micrometer and no corrections for thermal expansion of the cell were adopted.

The complex impedance ($Z^*(\omega) = Z'(\omega) + iZ''(\omega)$) is converted into complex conductivity ($\sigma^*(\omega) = \sigma'(\omega) + i\sigma''(\omega)$) and complex permittivity ($\varepsilon^*(\omega) = \varepsilon'(\omega) - i\varepsilon''(\omega)$) using the equations $\sigma^*(\omega) = k[Z^*(\omega)]^{-1}$ and $\varepsilon^*(\omega) = \sigma^*(\omega)/(i\omega\varepsilon_0)$, respectively, where k is the cell constant and $\omega = 2\pi f$ (f is the frequency in Hz).

Finally, the electric response of the material was quantitatively analyzed by simulating simultaneously the spectra of the $\varepsilon^*(\omega)$ and $\sigma^*(\omega)$ components and of $tan\ \delta(\omega)$ by Equations (5) and (6)

$$\varepsilon^*_m\ (\omega) = -i\left(\frac{\sigma_0}{\omega\varepsilon_0}\right)^N + \sum_{k=1}^{n}\frac{\sigma_k(i\omega\tau_k)^{\gamma_k}}{i\omega\varepsilon_0\left[1+(i\omega\tau_k)^{\gamma_k}\right]} + \sum_{i=1}^{m}\frac{\Delta\varepsilon_i}{\left[1+(i\omega\tau_i)^{a_i}\right]^{b_i}} + \varepsilon_\infty \tag{5}$$

$$\sigma*(\omega) = i\omega\varepsilon*(\omega)\ \text{ and }\ tan\ \delta\ (\omega) = \varepsilon''(\omega)/\varepsilon'(\omega) \tag{6}$$

where σ_0 is the residual conductivity of the material. σ_k the electrode (σ_{EP}) and the interdomain polarization conductivities ($\sigma_{IP,j}$, j = 1,2...) for k = EP or IP,j, respectively. τ_k and γ_k the relaxation time and an exponential factor of the k^{th} polarization. γ_k ranges from 0.5 to 1. The third term of Equation (5) corresponds to the dielectric relaxation phenomena.[43–45] $\Delta\varepsilon_i$, τ_i, α_i, and β_i are the dielectric strength, relaxation time ($\tau_i = \frac{1}{2\pi f_i}$) and shape

parameters (symmetric, and antisymmetric) of the i^{th} relaxation event, respectively. ε_∞ is the permittivity of the sample at an infinite frequency, i.e., associated with the electronic contribution of materials.

Supporting Information

Supporting Information is available from the Wiley Online Library or from the author.

Acknowledgements

K.V., C.T., and K.M. contributed equally to this work. Christoph Erdmann (Humboldt-Universität zu Berlin) is acknowledged for electron microscopy measurements.

Open access publishing facilitated by Universita degli Studi Mediterranea di Reggio Calabria, as part of the Wiley - CRUI-CARE agreement.

Conflict of Interest

The authors declare no conflict of interest.

Data Availability Statement

The data that support the findings of this study are available from the corresponding author upon reasonable request.

Keywords

electrocatalysts, High-entropy spinel oxides, hydrogen production, nanofibers, OER

Received: September 13, 2024
Revised: October 29, 2024
Published online:

[1] D. K. Bora, A. Braun, E. C. Constable, *Energy Environ. Sci.* **2013**, *6*, 407.
[2] R. D. Tentu, S. Basu, *Curr. Opin. Electrochem.* **2017**, *5*, 56.
[3] C. Meng, Y. Cao, Y. Luo, F. Zhang, Q. Kong, A. A. Alshehri, K. A. Alzahrani, T. Li, Q. Liu, X. Sun, *Inorg. Chem. Front.* **2021**, *8*, 3007.
[4] S. Wang, A. Lu, C. J. Zhong, *Nano Converg.* **2021**, *8*, 4.
[5] J. Yu, Q. He, G. Yang, W. Zhou, Z. Shao, M. Ni, *ACS Catal.* **2019**, *9*, 9973.
[6] F. Luo, L. Guo, Y. Xie, J. Xu, K. Qu, Z. Yang, *Appl. Catal. B* **2020**, *279*, 119394.
[7] Y. Li, Y. Sun, Y. Qin, W. Zhang, L. Wang, M. Luo, H. Yang, S. Guo, *Adv. Energy Mater.* **2020**, *10*, 1903120.
[8] M. Plevova, J. Hnat, K. Bouzek, *J. Power Sources* **2021**, *507*, 230072.
[9] J. N. Hansen, H. Prats, K. K. Toudahl, N. Mørch Secher, K. Chan, J. Kibsgaard, I. Chorkendorff, *ACS Energy Lett.* **2021**, *6*, 1175.
[10] A. Krishnan, R. Ajay, J. Anakha, U. K. Namboothiri, *Surf. Interfaces* **2022**, *30*, 101942.
[11] G. Shi, T. Tano, D. A. Tryk, M. Yamaguchi, A. Iiyama, M. Uchida, K. Iida, C. Arata, S. Watanabe, K. Kakinuma, *ACS Catal.* **2022**, *12*, 14209.
[12] X. Yang, S. Liping, L. Qiang, H. Lihua, Z. Hui, *J. Mater. Chem. A* **2022**, *10*, 17633.
[13] L. He, H. Kang, G. Hou, X. Qiao, X. Jia, W. Qin, X. Wu, *Chem. Eng. J.* **2023**, *460*, 141675.
[14] B. Talluri, K. Yoo, J. Kim, *J. Environ. Chem. Eng.* **2022**, *10*, 106932.
[15] S. Jiang, K. Tian, X. Li, C. Duan, D. Wang, Z. Wang, H. Sun, R. Zheng, Y. Liu, *J. Colloid Interfaces Sci.* **2022**, *606*, 635.
[16] F. Liu, M. Yu, X. Chen, J. Li, H. Liu, F. Cheng, *Chin. J. Catal.* **2022**, *43*, 122.
[17] K. H. Kim, Y. H. Choi, *J. Electroanal. Chem.* **2022**, *922*, 116737.
[18] Z. Sun, Y. Zhao, C. Sun, Q. Ni, C. Wang, H. Jin, *Chem. Eng. J.* **2022**, *431*, 133448.
[19] D. Stenzel, B. Zhou, C. Okafor, M. V. Kante, L. Lin, G. Melinte, T. Bergfeldt, M. Botros, H. Hahn, B. Breitung, S. Schweidler, *Front. Energy Res.* **2022**, *10*, 942314.
[20] M. Einert, M. Mellin, N. Bahadorani, C. Dietz, S. Lauterbach, J. P. Hofmann, *ACS Appl. Energy Mater.* **2022**, *5*, 717.
[21] C. Triolo, S. Schweidler, L. Lin, G. Pagot, V. Di Noto, B. Breitung, S. Santangelo, *Energy Adv.* **2023**, *2*, 667.
[22] M. Li, M. Song, W. Ni, Z. Xiao, Y. Li, J. Jia, S. Wang, Y. Wang, *Chin. Chem. Lett.* **2023**, *34*, 107571.
[23] J. Bao, X. Zhang, B. Fan, J. Zhang, M. Zhou, W. Yang, X. Hu, H. Wang, B. Pan, Y. Xie, *Angew. Chem.* **2015**, *127*, 7507.
[24] T. Liu, Z. Feng, Q. Li, J. Yang, C. Li, M. Dupuis, *Chem. Mater.* **2018**, *30*, 7714.
[25] K. Zhu, F. Shi, X. Zhu, W. Yang, *Nano Energy* **2020**, *73*, 104761.
[26] A. Badreldin, A. E. Abusrafa, A. Abdel-Wahab, *Emerg. Mater.* **2020**, *3*, 567.
[27] E. Marelli, J. Gazquez, E. Poghosyan, E. Müller, D. J. Gawryluk, E. Pomjakushina, D. Sheptyakov, C. Piamonteze, D. Aegerter, T. J. Schmidt, M. Medarde, E. Fabbri, *Angew. Chem.* **2021**, *60*, 14609.
[28] S. Roy, N. Devaraj, K. Tarafder, C. Chakraborty, S. Roy, *New J. Chem.* **2022**, *46*, 6539.
[29] C. Wei, Z. Feng, G. G. Scherer, J. Barber, Y. Shao-Horn, Z. J. Xu, *Adv. Mater.* **2017**, *29*, 1606800.
[30] S. Sun, Y. Sun, Y. Zhou, S. Xi, X. Ren, B. Huang, H. Liao, L. P. Wang, Y. Du, Z. J. Xu, *Angew. Chem.* **2019**, *131*, 6103.
[31] Y. Zhou, S. Sun, C. Wei, Y. Sun, P. Xi, Z. Feng, Z. J. Xu, *Adv. Mater.* **2019**, *31*, 1902509.
[32] J. Wang, S. Choi, J. Kim, S. W. Cha, J. Lim, *Catalysts* **2020**, *10*, 770.
[33] Y. Peng, C. Huang, J. Huang, M. Feng, X. Qiu, X. Yue, S. Huang, *Adv. Funct. Mater.* **2022**, *32*, 2201011.
[34] X. Li, Y. Sun, F. Ren, Y. Bai, Z. Cheng, *Mater. Today Energy* **2021**, *19*, 100619.
[35] Y. Xiao, Y. Wang, M. Xiao, C. Liu, S. Hou, J. Ge, W. Xing, *NPG Asia Mater.* **2020**, *12*, 73.
[36] T. Guo, L. Li, Z. Wang, *Adv. Energy Mater.* **2022**, *12*, 2200827.
[37] A. Ponti, C. Triolo, B. Petrovičovà, A. M. Ferretti, G. Pagot, W. Xu, V. Di Noto, N. Pinna, S. Santangelo, *Phys. Chem. Chem. Phys.* **2023**, *25*, 2212.
[38] X. Yin, J. Huang, Z. Pu, J. Li, H. Feng, X. Wang, Y. Wang, *Ceram. Int.* **2021**, *47*, 17167.
[39] A. Sarkar, B. Eggert, R. Witte, J. Lill, L. Velasco, Q. Wang, J. Sonar, K. Ollefs, S. S. Bhattacharya, R. A. Brand, H. Wende, F. M. F. de Grot, O. Clemens, H. Hahn, R. Kruk, *Acta Mater.* **2022**, *226*, 117581.
[40] A. Senthamizhan, B. Balusamy, Z. Aytac, T. Uyar, *CrystEngComm* **2016**, *18*, 6341.
[41] M. H. Elhousseini, T. Isik, Ö. Kap, F. Verpoort, N. Horzum, *Appl. Surf. Sci.* **2020**, *514*, 145939.
[42] F. Pantò, Z. Dahrouch, A. Saha, S. Patanè, S. Santangelo, C. Triolo, *Appl. Surf. Sci.* **2021**, *557*, 149830.
[43] V. Di Noto, G. A. Giffin, K. Vezzù, M. Piga, S. Lavina, in *Solid State Proton Conductors: Properties and Applications in Fuel Cells*, (Eds. P. Knauth, M. L. Di Vona), John Wiley & Sons, Weinheim, Germany **2012**, pp. 107–180;

[44] G. Pagot, F. Bertasi, G. Nawn, E. Negro, A. Bach Delpeuch, K. Vezzù, D. Cristofori, V. Di Noto, *Electrochim. Acta* **2017**, *225*, 533.
[45] K. Vezzù, E. García-González, G. Pagot, E. Urones-Garrote, M. E. Sotomayor, A. Varez, V. Di Noto, *Chem. Mater.* **2022**, *34*, 5484.
[46] M. Fiore, G. Longoni, S. Santangelo, F. Pantò, S. Stelitano, P. Frontera, P. Antonucci, R. Ruffo, *Electrochim. Acta* **2018**, *269*, 367.
[47] Y. Li, H. Zhang, X. Zhang, L. Wei, Y. Zhang, G. Hai, Y. Sun, *J. Mater. Sci.: Mater. Electron.* **2019**, *30*, 15734.
[48] F. Pantò, S. G. Leonardi, E. Fazio, P. Frontera, A. Bonavita, G. Neri, P. L. Antonucci, F. Neri, S. Santangelo, *Nanotechnology* **2018**, *29*, 305501.
[49] S. Santangelo, S. Patanè, P. Frontera, F. Pantò, C. Triolo, S. Stelitano, P. Antonucci, *Mater. Res. Bull.* **2017**, *92*, 9.
[50] D. Hu, R. Wang, P. Du, G. Li, Y. Wang, D. Fan, X. Pan, *Ceram. Int.* **2022**, *48*, 6549.
[51] C. Triolo, K. Moulaee, A. Ponti, G. Pagot, V. Di Noto, N. Pinna, G. Neri, S. Santangelo, *Adv. Funct. Mater.* **2024**, *34*, 2306375.
[52] L. Zheng, Y. Zhao, P. Xu, Y. Zhao, Z. Lv, W. Ye, X. Shi, Q. Wu, H. Zheng, *Chem. Eng. J.* **2023**, *456*, 140975.
[53] Q. Hu, Z. Wang, X. Huang, Y. Qin, H. Yang, X. Ren, Q. Zhang, J. Liu, C. He, *Energy Environ. Sci.* **2020**, *13*, 5097.
[54] A. Mao, F. Quan, H. Z. Xiang, Z. G. Zhang, K. Kuramoto, A. L. Xia, *J. Mol. Struct.* **2019**, *1194*, 11.
[55] T. X. Nguyen, J. Patra, J. K. Chang, J. M. Ting, *J. Mater. Chem. A* **2020**, *8*, 18963.
[56] D. Wang, S. Jiang, C. Duan, J. Mao, Y. Dong, K. Dong, Z. Wang, S. Luo, Y. Liu, X. Qi, *J. Alloys Compd.* **2020**, *844*, 156158.
[57] H. Chen, N. Qiu, B. Wu, Z. Yang, S. Sun, Y. Wang, *RSC Adv.* **2020**, *10*, 9736.
[58] M. Stygar, J. Dąbrowa, M. Moździerz, M. Zajusz, W. Skubida, K. Mroczka, K. Berent, K. Świerczek, M. Danielewski, *J. Eur. Cer. Soc.* **2020**, *40*, 1644.
[59] B. Liang, Y. Ai, Y. Wang, C. Liu, S. Ouyang, M. Liu, *Materials* **2020**, *13*, 5798.
[60] S. W. Oh, H. J. Bang, Y. C. Bae, Y. K. Sun, *J. Power Sources* **2007**, *173*, 502.
[61] H. D. Lutz, B. Müller, H. J. Steiner, *J. Solid St. Chem.* **1991**, *90*, 54.
[62] Z. Wang, R. T. Downs, V. Pischedda, R. Shetty, S. K. Saxena, C. S. Zha, Y. S. Zhao, D. Schiferl, A. Waskowska, *Phys. Rev. B* **2003**, *68*, 094101.
[63] V. D'Ippolito, G. B. Andreozzi, D. Bersani, P. P. Lottici, *J. Raman Spectrosc.* **2015**, *46*, 1255.
[64] P. Choudhary, D. Varshney, *Mater. Res. Express* **2017**, *4*, 076110.
[65] B. Nandan, M. C. Bhatnagar, S. C. Kashyap, *J. Phys. Chem. Solids* **2019**, *129*, 298.
[66] M. A. Laguna-Bercero, M. L. Sanjuán, R. I. Merino, *J. Phys.: Cond. Matter* **2007**, *19*, 186217.
[67] Z. Ž. Lazarević, Č. Jovalekić, A. Milutinović, D. Sekulić, V. N. Ivanovski, A. Rečnik, B. Cekič, N. Ž. Romčević, *J. Appl. Phys.* **2013**, *113*, 187221.
[68] M. H. Abdellatif, A. A. Azab, M. Salerno, *Mater. Res. Bull.* **2018**, *97*, 260.
[69] S. Supriya, S. Kumar, M. Kar, *J. Electron. Mater.* **2019**, *48*, 3612.
[70] W. Wang, Z. Ding, X. Zhao, S. Wu, F. Li, M. Yue, J. P. Liu, *J. Appl. Phys.* **2015**, *117*, 17A328.
[71] J. Dąbrowa, M. Stygar, A. Mikuła, A. Knapik, K. Mroczka, W. Tejchman, M. Danielewski, M. Martin, *Mater. Lett.* **2018**, *216*, 32.
[72] S. A. Patil, S. Cho, Y. Jo, N. K. Shrestha, H. Kim, H. Im, *Chem. Eng. J.* **2021**, *426*, 130773.
[73] S. Wahl, S. M. El-Refaei, A. G. Buzanich, P. Amsalem, K. S. Lee, N. Koch, M. L. Doublet, N. Pinna, *Adv. Energy Mater.* **2019**, *9*, 1900328.
[74] J. Kim, X. Yin, K. C. Tsao, S. Fang, H. Yang, *J. Am. Chem. Soc.* **2014**, *136*, 14646.
[75] H. B. Tao, L. Fang, J. Chen, H. B. Yang, J. Gao, J. Miao, S. Chen, B. Liu, *J. Am. Chem. Soc.* **2016**, *138*, 9978.
[76] V. I. Nefedov, Y. V. Salyn, G. Leonhardt, R. Scheibe, *J. Electron. Spectrosc. Relat. Phenomena* **1977**, *10*, 121.
[77] C. Triolo, M. Maisuradze, M. Li, Y. Liu, A. Ponti, G. Pagot, V. Di Noto, G. Aquilanti, N. Pinna, M. Giorgetti, S. Santangelo, *Small* **2023**, *19*, 2304585.
[78] T. J. Chuang, C. R. Brundle, D. W. Rice, *Surf. Sci.* **1976**, *59*, 413.
[79] K. S. Kim, N. Winograd, *Surf. Sci.* **1974**, *43*, 625.
[80] C. P. Li, A. Proctor, D. M. Hercules, *Appl. Spectrosc.* **1984**, *38*, 880.
[81] R. O. Ansell, T. Dickinson, A. F. Povey, *Corros. Sci.* **1978**, *18*, 245.
[82] E. Desimoni, C. Malitesta, P. G. Zambonin, J. C. Rivière, *Surf. Interface Anal.* **1988**, *13*, 173.
[83] V. Nefedov, D. Gati, B. Dzhurinskii, N. Sergushin, Y. V. Salyn, *J. Electron. Spectrosc. Relat. Phenomena* **1975**, *20*, 2307.
[84] B. Wichterlová, L. Krajčíková, Z. Tvarůžková, S. Beran, *J. Chem. Soc., Faraday Trans. 1* **1984**, *80*, 2639.
[85] J. P. Bonnelle, J. Grimblot, A. D'Huysser, *J. Electron. Spectrosc. Relat. Phenomena* **1975**, *7*, 151.
[86] G. Pagot, M. C. Cassani, F. Gambassi, B. Ballarin, D. Nanni, M. Coi, D. Barreca, E. Boanini, V. D. Noto, *Surf. Sci. Spectra* **2022**, *29*, 024007.
[87] B. R. Strohmeier, D. M. Hercules, *J. Catal.* **1984**, *86*, 266.
[88] J. Haber, J. Stoch, L. Ungier, *J. Electron Spectrosc. Relat. Phenomena* **1976**, *9*, 459.
[89] T. J. Frankcombe, Y. Liu, *Chem. Mater.* **2023**, *35*, 5468.
[90] B. J. Tan, K. J. Klabunde, P. M. Sherwood, *J. Am. Chem. Soc.* **1991**, *113*, 855.
[91] M. Virumbrales-del Olmo, A. Delgado-Cabello, A. Andrada-Chacón, J. Sánchez-Benítez, E. Urones-Garrote, V. Blanco-Gutiérrez, M. Torralvo, R. Sáez-Puche, *Phys. Chem. Chem. Phys.* **2017**, *19*, 8363.
[92] J. Tang, J. L. Xu, Z. G. Ye, X. B. Li, J. M. Luo, *J. Mater. Sci. Technol.* **2021**, *79*, 171.
[93] Y. Zhang, W. Dai, P. Zhang, T. Lu, Y. Pan, *J. Alloys Compd.* **2021**, *868*, 159064.
[94] E. O. Nwanebu, N. Abou Harb, R. Gharbi, S. Omanovic, *Solid State Sci.* **2021**, *119*, 106703.
[95] Y. Zhu, Q. Xiang, L. Guo, S. Lu, F. Duan, M. Du, H. Zhu, *Colloids Surf. A* **2024**, *686*, 133315.
[96] G. Buvat, M. J. Eslamibidgoli, A. H. Youssef, S. Garbarino, A. Ruediger, M. Eikerling, D. Guay, *ACS Catal.* **2020**, *10*, 806.
[97] M. Harada, F. Kotegawa, M. Kuwa, *ACS Appl. Energy Mater.* **2022**, *5*, 278.
[98] V. Di Noto, G. Pagot, K. Vezzù, E. Negro, P. Sgarbossa, in *Electrocatalysis for Membrane Fuel Cells: Methods, Modeling and Applications*, Wiley-VCH, Weinheim, Germany **2023**, pp. 69–109.
[99] X. Chen, Z. Zhang, Y. Chen, R. Xu, C. Song, T. Yuan, W. Tang, X. Gao, N. Wang, L. Cui, *Energy Mater.* **2023**, *3*, 300044.
[100] J. Sun, N. Guo, Z. Shao, K. Huang, Y. Li, F. He, Q. Wang, *Adv. Energy Mater.* **2018**, *8*, 1800980.
[101] H. Chen, L. Shi, X. Liang, L. Wang, T. Asefa, X. Zou, *Angew. Chem.* **2020**, *59*, 19654.
[102] Y. Sun, H. Liao, J. Wang, B. Chen, S. Sun, S. J. H. Ong, S. Xi, C. Diao, Y. Du, J. O. Wang, M. B. H. Breese, S. Li, H. Zhang, Z. J. Xu, *Nat. Catal.* **2020**, *3*, 554.
[103] A. Badreldin, A. E. Abusrafa, A. Abdel-Wahab, *ChemSusChem* **2021**, *14*, 10.
[104] D. Briggs, M. P. Seah, *Practical Surface Analysis: Auger and X-Ray Photoelectron Spectroscopy*, John Wiley & Sons, New York, **1990**.
[105] D. A. Shirley, *Phys. Rev. B* **1972**, *5*, 4709.
[106] S. Q. Chang, C. C. Cheng, P. Y. Cheng, C. L. Huang, S. Y. Lu, *Chem. Eng. J.* **2022**, *446*, 137452.
[107] L. Danyang, S. Liping, L. Qiang, X. Tian, H. Lihua, Z. Hui, *J. Alloys Compd.* **2022**, *913*, 165148.